
Article:
Karageorghis, A, Lesnic, D orcid.org/0000-0003-3025-2770 and Marin, L (2018) The method of fundamental solutions for the identification of a scatterer with impedance boundary condition in interior inverse acoustic scattering. Engineering Analysis with Boundary Elements, 92. pp. 218-224. ISSN 0955-7997

https://doi.org/10.1016/j.enganabound.2017.07.005

THE METHOD OF FUNDAMENTAL SOLUTIONS FOR THE IDENTIFICATION OF A SCATTERER WITH IMPEDANCE BOUNDARY CONDITION IN INTERIOR INVERSE ACOUSTIC SCATTERING

A. KARAGEORGHIS, D. LESNIC, AND L. MARIN

Abstract. We employ the method of fundamental solutions (MFS) for detecting a scatterer surrounding a host acoustic homogeneous medium D due to a given point source inside it. On the boundary of the unknown scatterer (assumed to be star-shaped), allowing for the normal velocity to be proportional to the excess pressure, a Robin impedance boundary condition is considered. The coupling Robin function λ may or may not be known. The additional information which is supplied in order to compensate for the lack of knowledge of the boundary ∂D of the interior scatterer D and/or the function λ is given by the measurement of the scattered field (generated by the interior point source) on a curve inside D. These measurements may be contaminated with noise so their inversion requires regularization. This is enforced by minimizing a penalised least-squares functional containing various regularization parameters to be prescribed. In the MFS, the unknown scattered field u^s is approximated with a linear combination of fundamental solutions of the Helmholtz operator with their singularities excluded from the solution domain D and this yields the discrete version of the objective functional. Physical constraints are added and the resulting constrained minimization problem is solved using the MATLAB© toolbox routine `lsqnonlin`. Numerical results are presented and discussed.

1. Introduction

Recently, the interior inverse scattering problem initiated in [6] for testing the structural integrity of a cavity has received some attention [17, 18, 21] due to its potential practical importance and pathway to impact proposed in [17] to model the calculation of the extent of a homogeneous reservoir from the measured data obtained from a transmitter-receiver instrument which is lowered through a borehole into the reservoir.

The numerical reconstruction of a sound-soft, i.e. perfectly conducting scatterer D on whose boundary ∂D the total field u vanishes, from measurements on an interior closed curve Γ inside D was previously investigated as follows:

- in [17], using the boundary element method (BEM) based on the single layer potential representation for the scattered field u^s and a regularized Newton minimization method;
- in [18], using the BEM based on the double layer potential representation for u^s and the linear sampling method;
- in [21], using a decomposition method based on a variant of the method of fundamental solutions (MFS), see [4, 11], combined with a simple graphical method based on plotting the zero level set contours of the total field;
- in [9, 10], using the MFS (or the plane waves method (PWM)) combined with a trust region reflective algorithm for minimizing the nonlinear Tikhonov regularization functional subject to constraints, implemented using the MATLAB© toolbox routine `lsqnonlin`.

Later on, the linear sampling method and the factorization method were employed in [19, 15], respectively, to reconstruct a scatterer on whose boundary a homogeneous Robin boundary condition is satisfied by the total field. It is the purpose of this paper to extend the MFS analysis of [9] for the sound-soft scatterer to the more general identification of a scatterer with a Robin boundary condition which includes the sound-hard case of a perfectly

Date: July 19, 2017.

2010 *Mathematics Subject Classification.* Primary 65N35; Secondary 65N21, 65N38.

Key words and phrases. Method of fundamental solutions; Interior inverse scattering; Impedance boundary condition; regularization.

insulated scatterer when $\lambda = 0$ and the sound-soft case of a perfectly conducting scatterer when $\lambda = \infty$. Moreover, the coupling function λ between the Dirichlet and Neumann data in the Robin boundary condition may be known or unknown. Therefore, we shall investigate three inverse problems: Problem A in which D is unknown but λ is known, problem B in which D is known but λ is unknown, and problem C in which both D and λ are unknown.

The plan of the paper is as follows. In Section 2, we present the formulations of the direct and inverse problems that are investigated. The MFS approximation of the scattered field and the numerical realization of the constrained nonlinear minimization problem are described in Section 3. Numerical results are analyzed and discussed in terms of accuracy and stability in Section 4. In particular, the influence of the regularization parameters on the stability of the reconstructions of the scatterer D and/or the Robin function λ are thoroughly investigated. Finally, conclusions and possible future work are included in Section 5.

2. Mathematical formulation

We consider the scattering with a wave number $0 < k = \omega/c$, where $c > 0$ is the speed of sound and $\omega > 0$ is the frequency of a time harmonic wave, due to a given point source $\boldsymbol{z}_0$ inside the two-dimensional, bounded and simply-connected scatterer domain D with a sufficiently smooth, e.g. C^2, [19], or Lipschitz, [15], boundary ∂D. Then the incident field is given by

$$u^{\rm inc}(\boldsymbol{x}) = \Phi(\boldsymbol{x}, \boldsymbol{z}_0) := \frac{\rm i}{4} H_0^{(1)}(k|\boldsymbol{x} - \boldsymbol{z}_0|), \quad \boldsymbol{x} \in \mathbb{R}^2, \tag{2.1}$$

where i is the imaginary unit and $H_0^{(1)}$ denotes the Hankel function of first kind of order zero, and the scattered field $u^{\rm s}$ satisfies the Helmholtz equation

$$\Delta u^{\rm s} + k^2 u^{\rm s} = 0 \quad \text{in} \quad D. \tag{2.2}$$

Plane wave propagation in a given direction or an incoming cylindrical wave [13, 14], can also be considered instead of the point source wave (2.1).

On the boundary ∂D of D we assume that a homogeneous Robin boundary condition for the total field $u = u^{\rm s} + u^{\rm inc}$ holds, namely,

$$\frac{\partial u}{\partial \nu} + {\rm i}\,\lambda\, u = 0, \quad \text{on} \quad \partial D, \tag{2.3}$$

where $\boldsymbol{\nu}$ is the outward unit normal to ∂D and $0 < \lambda \in C(\partial D)$ or $L^\infty(\partial D)$ is a Robin coupling real function usually called the impedance function, [15], or admittance, [8]. When $\lambda \to 0$ or $\lambda \to \infty$ we obtain the particular cases of a sound-hard or sound-soft scatterer, respectively. However, unlike these ideal cases, the Robin impedance boundary condition (2.3) with $0 < \lambda < \infty$ is more realistic because, in practice, scatterers are never perfect and the waves always penetrate a little through the boundary ∂D, with λ characterising the level of penetration.

Using (2.1) we can recast (2.3) as a non-homogeneous Robin boundary condition for the scattered field given by

$$\frac{\partial u^{\rm s}}{\partial \nu}(\boldsymbol{x}) + {\rm i}\,\lambda\, u^{\rm s}(\boldsymbol{x}) = \frac{k\,{\rm i}}{4} H_1^{(1)}(k|\boldsymbol{x} - \boldsymbol{z}_0|)\, \frac{(\boldsymbol{x} - \boldsymbol{z}_0)\cdot \boldsymbol{\nu}(\boldsymbol{x})}{|\boldsymbol{x} - \boldsymbol{z}_0|} + \frac{\lambda}{4}\, H_0^{(1)}(k|\boldsymbol{x} - \boldsymbol{z}_0|), \quad \boldsymbol{x} \in \partial D, \tag{2.4}$$

where $H_1^{(1)}$ is the Hankel function of the first kind of order one.

2.1. The direct problem.

When D and λ are known, equations (2.2) and (2.4) form the direct problem which is well-posed in $C^2(D) \cap C^1(\overline{D})$ or $H^1(D)$, [2, 3]. In the case of the Dirichlet ($\lambda \to 0$) or Neumann ($\lambda \to \infty$) boundary conditions we need to add the assumption that k^2 is not a Dirichlet or Neumann eigenvalue of $-\Delta$ in D, respectively.

2.2. The inverse problems.

We consider the following inverse problems under the general assumption that:
(α) k^2 is not a Dirichlet eigenvalue for $-\Delta$ in the interior Ω of the curve Γ introduced below. Note however that this assumption is not so essential as we can always rescale Γ, [21].

2.2.1. *Inverse problem* A. Solve the Helmholtz equation (2.2) for the scattered field $u^{\rm s}$ subject to the Robin boundary condition (2.4) with given λ but unknown boundary ∂D which also has to be determined from additional measurements of $u^{\rm s}$ on some known interior closed curve Γ assumed to lie inside D. The condition that $\boldsymbol{z}_0 \in \Gamma$ is not essential but in the sequel we shall assume, for simplicity, that Γ is the circle of radius $|\boldsymbol{z}_0| > 0$ centred at the origin, i.e.

$$\Gamma = \partial B_{|\boldsymbol{z}_0|}(\boldsymbol{0}). \tag{2.5}$$

Then the above additional condition is

$$u^{\rm s}(\boldsymbol{x}) \,=\, f(\boldsymbol{x}), \quad \boldsymbol{x} \,\in\, \Gamma, \tag{2.6}$$

where f is some given measured data which may be contaminated with noise.

2.2.2. *Inverse problem* B. In this case we again consider the Helmholtz equation (2.2) for the scattered field $u^{\rm s}$ subject to the Robin boundary condition (2.4) but now the boundary ∂D is known and the impedance $\lambda(\boldsymbol{x})$ is unknown. The additional measurements are again given by (2.6).

2.2.3. *Inverse problem* C. Now both the boundary ∂D and the impedance $\lambda(\boldsymbol{x})$ in (2.4) are unknown.

At this stage, we briefly discuss the way the data f, obtained from the measurement of the scattered field Γ, could be interpreted. We first observe that the data f in expression (2.6) is rather limited because it only contains the measurement obtained from a single point source $\boldsymbol{z}_0 \in D$. Also, (2.6) can be further restricted to a limited aperture case by only specifying it on a subportion Γ_1 of Γ. We have also fixed the wave number k. So, we can remark that in some practical applications it may be possible to measure more data obtained by varying the wave number k or the point source $\boldsymbol{z}_0$ along Γ. Thus, in general, for compatible data the function f in (2.6) depends on both $\boldsymbol{z}_0$ and k. In particular, for fixed k satisfying assumption (α), but varying $\boldsymbol{z}_0 \in \Gamma$ so that (2.6) reads as a matrix of measured data

$$u^{\rm s}(\boldsymbol{x}; \boldsymbol{z}_0) \,=\, f(\boldsymbol{x}; \boldsymbol{z}_0), \quad \boldsymbol{x}, \boldsymbol{z}_0 \,\in\, \Gamma, \tag{2.7}$$

then a solution of inverse problem C given by (2.2), (2.4) and (2.7) is unique, [19]. However, this uniqueness result requires the measurement $u^{\rm s}(\cdot; \boldsymbol{z}_0)$ for infinitely many point sources $\boldsymbol{z}_0 \in \Gamma$ which may become impractical. We note that for a single fixed source $\boldsymbol{z}_0 \in \Gamma$, the uniqueness of the restricted inverse problem A given by (2.2), (2.4) and (2.6) is only known when we assume *a priori* that D is a disk, [15], a small and smooth perturbation of a disk, [12], or in the sound-soft case ($\lambda \to \infty$), by requiring D to be contained in a disk of radius t_0/k, where $t_0 = 2.40482$ is the smallest positive zero of the Bessel function J_0.
On first solving the direct well-posed Dirichlet problem for the Helmholtz equation given by (2.2) in Ω and (2.6), with assumption (α), the normal derivative

$$\frac{\partial u^{\rm s}}{\partial \nu}(\boldsymbol{x}) =: g(\boldsymbol{x}), \quad \boldsymbol{x} \in \Gamma, \tag{2.8}$$

can be obtained. It then means that (2.6) and (2.8) are compatible Cauchy data for the Helmholtz equation (2.2) in the annular domain $D \backslash \Omega$. From the unique continuation property of the Helmholtz equation it follows that the Cauchy data $u^{\rm s}$ and $\partial_\nu u^{\rm s}$ on ∂D are uniquely determined. Then, in principle, provided that $u \neq 0$ almost everywhere on ∂D the coefficient λ could be determined directly from (2.3) as

$$\lambda(\boldsymbol{x}) = {\rm i}\, \frac{\partial_\nu u(\boldsymbol{x})}{u(\boldsymbol{x})}, \quad \boldsymbol{x} \in \partial D. \tag{2.9}$$

However, this direct method was found to be less accurate and stable than a regularized nonlinear least-squares method based on approximating λ with a finite linear combination of trigonometric functions, [19].

3. The method of fundamental solutions (MFS)

In the MFS we seek the solution of the inverse Helmholtz problem (2.2), (2.4) and (2.6) in the form, see e.g. [5],

$$u_M^{\rm s}(\boldsymbol{x}) = \sum_{m=1}^{M} c_m\, G(\boldsymbol{x}, \boldsymbol{y}_m), \qquad \boldsymbol{x} \in \overline{D}, \tag{3.1}$$

where $\boldsymbol{y}_m \in \mathbb{R}^2 \backslash \overline{D}$ are singularities and $c_m \in \mathbb{C}$ are unknown complex coefficients to be determined by imposing boundary condition (2.4) and condition (2.6). Moreover, G is the fundamental solution of the two-dimensional Helmholtz operator given by [5]

$$G(\boldsymbol{x}, \boldsymbol{y}) = \frac{\rm i}{4}\, H_0^{(1)}(k|\boldsymbol{x} - \boldsymbol{y}|). \tag{3.2}$$

3.1. **Inverse problem A.** We assume that the unknown boundary ∂D is a smooth, star-like curve with respect to the origin. This means that its equation in polar coordinates can be written as

$$x = r(\vartheta)\cos\vartheta, \qquad y = r(\vartheta)\sin\vartheta, \qquad \vartheta \in [0, 2\pi), \tag{3.3}$$

where r is a smooth $2\pi-$periodic function.
The outward unit normal $\boldsymbol{\nu}(\boldsymbol{x})$ to ∂D at the point $\boldsymbol{x}$ is defined as

$$\boldsymbol{\nu}(\boldsymbol{x}) = \frac{1}{\sqrt{r^2(\vartheta) + r'^2(\vartheta)}} \Big(r'(\vartheta)\sin\vartheta + r(\vartheta)\cos\vartheta,\, r(\vartheta)\sin\vartheta - r'(\vartheta)\cos\vartheta \Big). \tag{3.4}$$

If we let $\vartheta_m = 2\pi(m-1)/M$ for $m = \overline{1, M}$, be a uniform discretization of the interval $[0, 2\pi)$, then the discretized form of (3.3) for ∂D becomes

$$r_m = r(\vartheta_m), \quad m = \overline{1, M}. \tag{3.5}$$

In (3.4), we use the finite-difference approximation

$$r'(\vartheta_i) \approx \frac{r_{i+1} - r_{i-1}}{4\pi/M}, \quad i = \overline{1, M}, \tag{3.6}$$

with the convention that $r_{M+1} = r_1$, $r_0 = r_M$.
On the unknown star-shaped boundary ∂D we consider the points

$$\boldsymbol{x}_m = r_m \left(\cos\vartheta_m, \sin\vartheta_m\right), \qquad m = \overline{1, M}, \tag{3.7}$$

expressed in polar coordinates, where the radii $r_m > 0$ are unknown. The MFS singularities are taken to be

$$\boldsymbol{y}_m = \eta\, r_m \left(\cos\vartheta_m, \sin\vartheta_m\right), \qquad m = \overline{1, M}, \tag{3.8}$$

where $\eta > 1$ is an unknown magnification parameter to be determined as part of the solution, see the description of the moving pseudo-boundary MFS in [7]. The measured data (2.6) are given at the points on the circle Γ, see (2.5),

$$\tilde{\boldsymbol{x}}_\ell = |\boldsymbol{z}_0| \left(\cos\varphi_\ell, \sin\varphi_\ell\right), \quad \varphi_\ell = 2\pi(\ell - 1)/L, \quad \ell = \overline{1, L}. \tag{3.9}$$

We thus have $3M + 1$ unknowns, namely the radii $\boldsymbol{r} = (r_m)_{m=\overline{1,M}}$, the complex coefficients $\boldsymbol{c} = (c_m)_{m=\overline{1,M}}$ and the magnification parameter η in (3.8). These are determined by imposing the (complex) boundary condition (2.1) at the M points $(\boldsymbol{x}_m)_{m=1}^{M}$ which yield $2M$ equations, and by imposing the (complex) condition (2.6) at the L points $(\tilde{\boldsymbol{x}}_\ell)_{\ell=1}^{L}$ which yield an additional $2L$ equations. We thus have $2M + 2L$ equations in $3M + 1$ unknowns and therefore need to take $2L \geq M + 1$.

To obtain a stable approximation to the inverse problem, we minimize the regularized nonlinear least-squares functional

$$T_{\mu_1,\mu_2}(\boldsymbol{c},\boldsymbol{r},\eta) := \sum_{m=1}^{M}\left|\sum_{j=1}^{M} c_j\,\left(\frac{\partial G}{\partial \nu}(\boldsymbol{x}_m,\boldsymbol{y}_j)+\mathrm{i}\,\lambda(\boldsymbol{x}_m)\,G(\boldsymbol{x}_m,\boldsymbol{y}_j)\right)\right.$$
$$\left.-\frac{k\,\mathrm{i}}{4}H_1^{(1)}(k|\boldsymbol{x}_m-\boldsymbol{z}_0|)\frac{(\boldsymbol{x}_m-\boldsymbol{z}_0)\cdot\boldsymbol{\nu}(\boldsymbol{x}_m)}{|\boldsymbol{x}_m-\boldsymbol{z}_0|}-\frac{\lambda(\boldsymbol{x}_m)}{4}H_0^{(1)}(k|\boldsymbol{x}_m-\boldsymbol{z}_0|)\right|^2$$
$$+\sum_{\ell=1}^{L}\left|\sum_{j=1}^{M} c_j\,G(\tilde{\boldsymbol{x}}_\ell,\boldsymbol{y}_j)-f^{\varepsilon}(\tilde{\boldsymbol{x}}_\ell)\right|^2+\mu_1\sum_{j=1}^{M}|c_j|^2+\mu_2\sum_{m=2}^{M}(r_m-r_{m-1})^2, \tag{3.10}$$

where $\mu_1,\mu_2\geq 0$ are regularization parameters, subject to the simple bounds on the variables

$$|\boldsymbol{z}_0|<r_m,\quad m=\overline{1,M},\quad \text{and}\quad 1<\eta<2. \tag{3.11}$$

In the case of a sound-soft or sound-hard scatterer an upper bound on r_m can be imposed as $2.4048/k$ or $P_{1,1}/k$, respectively, [12], where $P_{1,1}=1.8412$ is the smallest positive zero of the function J_1'.
The data (2.6) come from practical measurements which are inherently contaminated with errors due to noise, and we therefore replace f by f^{ε}, and in computation, the noisy data are generated as

$$f^{\varepsilon}(\tilde{\boldsymbol{x}}_\ell)=(1+\rho_\ell\,p)\,f(\tilde{\boldsymbol{x}}_\ell)\,,\quad \ell=\overline{1,L}\,, \tag{3.12}$$

where p represents the percentage of noise added to the data (2.6) on Γ, and ρ_ℓ is a pseudo-random noisy variable drawn from a uniform distribution in $[-1,1]$ using the MATLAB© [16] command `-1+2*rand(1,L)`. The way the noisy data is generated or its type (multiplicative uniform or additive Gaussian) is not important, as our analysis does not need to assume anything about the statistical properties of the noise.
The first sum in (3.10) corresponds to the satisfaction of boundary condition (2.4), whereas the second sum corresponds to the perturbed (3.12) internal measurement condition (2.6). Since the inverse problem is ill-posed, in (3.10), the regularization terms $\mu_1\sum_{j=1}^{M}|c_j|^2$ and $\mu_2\sum_{m=2}^{M}(r_m-r_{m-1})^2$ are added in order to achieve the stability of the MFS approximation u_M^{s} and of the smooth boundary ∂D.

The above constrained optimization problem (3.10) and (3.11) is solved using the MATLAB© toolbox routine `lsqnonlin` which does not require supplying the gradient of the functional (3.10) and easily incorporates the constraints (3.11). The fundamental solution (3.2) is calculated using the MATLAB© function `besselh`. In the implementation of `lsqnonlin` for the first set of constraints in (3.11) we set the lower and upper bounds `lb` and `ub` on r_m to be $|\boldsymbol{z}_0|+10^{-3}$ and 100, respectively.

3.2. **Inverse problem B.** In this case the boundary ∂D is known and we assume it may be described by (3.3), where r is a known smooth $2\pi-$periodic function. Since r is now known, we may calculate r' and hence $\boldsymbol{\nu}(\boldsymbol{x})$ from (3.4). If the (now known) collocation points are given by (3.7) and the corresponding singularities by (3.8), we still consider $\eta>1$ to be unknown. Since now the impedance $\lambda(\boldsymbol{x})$ is unknown we discretize it using

$$\lambda_m=\lambda(\vartheta_m),\quad m=\overline{1,M}. \tag{3.13}$$

We thus still have $3M+1$ unknowns, namely the $\boldsymbol{\lambda}=(\lambda_m)_{m=\overline{1,M}}$, the complex coefficients $\boldsymbol{c}=(c_m)_{m=\overline{1,M}}$ and the magnification parameter η in (3.8). These are determined, as before, by imposing the (complex) boundary condition (2.1) at the M points $(\boldsymbol{x}_m)_{m=1}^{M}$ which yield $2M$ equations, and by imposing the (complex) condition (2.6) at the L points $(\tilde{\boldsymbol{x}}_\ell)_{\ell=1}^{L}$ which yield an additional $2L$ equations. We thus have $2M+2L$ equations in $3M+1$ unknowns and therefore need to take $2L\geq M+1$.

We now minimize the regularized nonlinear least-squares functional

$$T_{\mu_1,\mu_2}(\boldsymbol{c},\boldsymbol{\lambda},\eta) := \sum_{m=1}^{M}\left|\sum_{j=1}^{M} c_j\,\left(\frac{\partial G}{\partial \nu}(\boldsymbol{x}_m,\boldsymbol{y}_j)+\mathrm{i}\,\lambda_m\,G(\boldsymbol{x}_m,\boldsymbol{y}_j)\right)\right.$$
$$\left.-\frac{k\,\mathrm{i}}{4}H_1^{(1)}(k|\boldsymbol{x}_m-\boldsymbol{z}_0|)\frac{(\boldsymbol{x}_m-\boldsymbol{z}_0)\cdot\boldsymbol{\nu}(\boldsymbol{x}_m)}{|\boldsymbol{x}_m-\boldsymbol{z}_0|}-\frac{\lambda_m}{4}H_0^{(1)}(k|\boldsymbol{x}_m-\boldsymbol{z}_0|)\right|^2$$
$$+\sum_{\ell=1}^{L}\left|\sum_{j=1}^{M} c_j\,G(\tilde{\boldsymbol{x}}_\ell,\boldsymbol{y}_j)-f^{\varepsilon}(\tilde{\boldsymbol{x}}_\ell)\right|^2+\mu_1\sum_{j=1}^{M}|c_j|^2+\mu_3\sum_{m=2}^{M}(\lambda_m-\lambda_{m-1})^2, \tag{3.14}$$

where $\mu_1,\mu_3\geq 0$ are regularization parameters, subject to the simple bounds on the variables

$$0<\lambda_m,\quad m=\overline{1,M},\quad \text{and}\quad 1<\eta<2. \tag{3.15}$$

In the implementation of `lsqnonlin` for the first set of constraints in (3.15) we set the lower and upper bounds `lb` and `ub` on λ_m to be 10^{-3} and 100, respectively.

3.3. **Inverse problem C.** In this case both the boundary ∂D and the impedance $\lambda(\boldsymbol{x})$ are unknown. The boundary ∂D is assumed to be star-like and described by (3.3) with its discretized form given by (3.5). The remaining discretization details are as in Section 3.1. Similarly, the discretized form of the impedance is given by (3.13).

Now we have $4M+1$ unknowns, namely the radii $\boldsymbol{r}=(r_m)_{m=\overline{1,M}}$, the $\boldsymbol{\lambda}=(\lambda_m)_{m=\overline{1,M}}$, the complex coefficients $\boldsymbol{c}=(c_m)_{m=\overline{1,M}}$ and the magnification parameter η in (3.8). These are determined, as before, by imposing the (complex) boundary condition (2.1) at the M points $(\boldsymbol{x}_m)_{m=1}^{M}$ which yield $2M$ equations, and by imposing the (complex) condition (2.6) at the L points $(\tilde{\boldsymbol{x}}_\ell)_{\ell=1}^{L}$ which yield an additional $2L$ equations. We thus have $2M+2L$ equations in $4M+1$ unknowns and therefore need to take $2L\geq 2M+1$.

We now minimize the regularized nonlinear least-squares functional

$$T_{\mu_1,\mu_2,\mu_3}(\boldsymbol{c},\boldsymbol{r},\boldsymbol{\lambda},\eta) := \sum_{m=1}^{M}\left|\sum_{j=1}^{M} c_j\,\left(\frac{\partial G}{\partial \nu}(\boldsymbol{x}_m,\boldsymbol{y}_j)+\mathrm{i}\,\lambda_m\,G(\boldsymbol{x}_m,\boldsymbol{y}_j)\right)\right.$$
$$\left.-\frac{k\,\mathrm{i}}{4}H_1^{(1)}(k|\boldsymbol{x}_m-\boldsymbol{z}_0|)\frac{(\boldsymbol{x}_m-\boldsymbol{z}_0)\cdot\boldsymbol{\nu}(\boldsymbol{x}_m)}{|\boldsymbol{x}_m-\boldsymbol{z}_0|}-\frac{\lambda_m}{4}H_0^{(1)}(k|\boldsymbol{x}_m-\boldsymbol{z}_0|)\right|^2$$
$$+\sum_{\ell=1}^{L}\left|\sum_{j=1}^{M} c_j\,G(\tilde{\boldsymbol{x}}_\ell,\boldsymbol{y}_j)-f^{\varepsilon}(\tilde{\boldsymbol{x}}_\ell)\right|^2+\mu_1\sum_{j=1}^{M}|c_j|^2+\mu_2\sum_{m=2}^{M}(r_m-r_{m-1})^2+\mu_3\sum_{m=2}^{M}(\lambda_m-\lambda_{m-1})^2, \tag{3.16}$$

where $\mu_1,\mu_2,\mu_3\geq 0$ are regularization parameters, subject to the simple bounds (3.11) and (3.15).

4. Numerical results and discussion

We take, for simplicity, the wave number k equal to unity. In (3.10), (3.14) and (3.16) we take only one of the regularization parameters μ_1,μ_2 and μ_3 to be non-zero and investigate all the possibilities that may occur by trial and error. This is not based on knowing the exact solution but on trying various values of the regularization parameter starting with large values, which will oversmooth the obtained scatterer, and decreasing it to lower values until instability, i.e. the scatterer becomes unbounded and oscillatory, starts to manifest. In addition, taking more than one of these regularization parameters to be non-zero complicates their selection which could be accomplished within the generalized L-curve framework of [1]. A sample of the L-curve application is actually presented in Figure 4 for inverse problem A of Example 1.

In all figures presented in this section, the blue curves represent the exact solutions (for D and/or λ) and the red dots represent the numerical reconstructions.

4.1. **Example 1.** We first consider the simple case of a circular scatterer D of unit radius. We take $\boldsymbol{z}_0 = (0.5, 0)$,

$$\lambda(\vartheta) = 2 - \cos\vartheta, \quad \vartheta \in [0, 2\pi), \tag{4.1}$$

and the measured data on Γ are simulated by solving the direct problem (2.2) and (2.4) using the MFS with $\mathcal{M} = 60$ collocation points, $\mathcal{N} = 40$ singularities on a fixed pseudo-boundary similar to the physical boundary with a magnification factor of $\eta = 1.2$. The data (2.6) were generated at $L = 32$ points on Γ.

4.1.1. *Inverse problem* A. In the implementation of this inverse problem we took the initial guess $(\boldsymbol{c}^0, \boldsymbol{r}^0, \eta^0) = (\mathbf{0}, \mathbf{0.6}, 1.5)$ and $M = 50$. In Figure 1 we present the reconstructed boundary with no noise and no regularization after $1, 50, 100$ and 500 iterations (`niter`). From this figure it can be seen that there is a very good agreement between the exact and numerical solutions for `niter`=500. The CPU times recorded for various numbers of iterations using MATLAB© on a desktop PC (i7-6700 processor, CPU@3.40 GHZ, 16 GB memory) are presented in Table 1. The CPU times required for all subsequent calculations in this study were similar.

`niter`	100	200	300	400	500
CPU time (secs)	46	93	146	203	245

TABLE 1. Example 1: Typical CPU times for various numbers of iterations.

The corresponding results with `niter`=500, noise $p = 5\%$, $\mu_2 = 0$ and regularization with μ_1, and $\mu_1 = 0$ and regularization with μ_2, are presented in Figures 2 and 3, respectively. From these figures the following conclusions can be deduced:

– the numerical results without regularization are unstable;
– regularization with μ_1 between 10^{-2} and 10^{-1} achieves stable and accurate numerical results.
– regularization with μ_2 between 10^0 and 10^1 achieves stable and accurate numerical results.

The L-curves corresponding to the above two cases are presented in Figure 4. From Figure 4(a) it may be seen that the corner of the L-curve corresponds to $\mu_1 = 10^{-2}$ to 10^{-1} which is consistent with the results presented in Figure 2. From Figure 4(b) we observe that the corner of the L-curve corresponds to $\mu_2 = 1$ to $\mu_2 = 10$ which is consistent with the results presented in Figure 3.

4.1.2. *Inverse problem* B. In the implementation of this inverse problem we took the initial guess $(\boldsymbol{c}^0, \boldsymbol{\lambda}^0, \eta^0) = (\mathbf{0}, \mathbf{1}, 1.5)$ and $M = 50$. In Figure 5 we present the reconstructed impedance $\lambda(\vartheta)$ with no noise and no regularization after $1, 5, 100$ and 500 iterations and convergent results to the exact solution (4.1) for $\lambda(\vartheta)$ can be observed. The corresponding results with `niter`=500, noise $p = 5\%$, $\mu_3 = 0$ and regularization with μ_1, and $\mu_1 = 0$ and regularization with μ_3, are presented in Figures 6 and 7, respectively. We observe that when $p = 5\%$ noise is considered in the input data (3.12), the numerical solution is unstable if no regularization is imposed in (3.14). In order to achieve stable reconstructions of the coefficient λ, regularization with $\mu_1 = 10^{-1}$, $\mu_3 = 0$ (Figure 6) or with $\mu_1 = 0$, $\mu_3 = 10^{-3}$ (Figure 7) recovers stably the exact solution (4.1).

4.1.3. *Inverse problem* C. In the implementation of this inverse problem we took the initial guess $(\boldsymbol{c}^0, \boldsymbol{r}^0, \boldsymbol{\lambda}^0, \eta^0) = (\mathbf{0}, \mathbf{0.8}, \mathbf{1.2}, 1.5)$ and $M = 25$. We have taken $M = 25$ instead of $M = 50$ because for inverse problem C, for the overdetermination of the number of equations with respect to the number of unknowns, we need to have $2L \geq 2M + 1$ (see Section 3.3), whilst for inverse problems A and B we only need to have $2L \geq M + 1$ (see Sections 3.1 and 3.2). Initially, the same initial guesses for $\boldsymbol{r}^0 = 0.6$ and $\boldsymbol{\lambda}^0 = 1$ as those for problems A and B, respectively, were chosen for problem C, but the results obtained were not in good agreement with the sought solution given by (4.1) for the impedance function and by the unit disk for the scatterer. An explanation for this is that the gradient-based iterative routine `lsqnonlin` could have been stuck in a local minimum. In addition, as discussed

in Section 2.2.3, it is likely that solving problem C with measured data (2.6) from only a single point source $\boldsymbol{z}_0$ formulates an inverse problem with a non-unique solution and therefore, the numerical reconstruction (without noise and no regularization) would be biased towards the closest solution to the initial guess. Taking data (2.6) obtained from more point sources $\boldsymbol{z}_0 \in \Gamma$ would alleviate the non-uniqueness issue or, imposing regularization, as in (3.16), will pick the solution closest to the origin. Alternatively, we take an initial guess $\boldsymbol{r}^0 = 0.8$ and $\boldsymbol{\lambda}^0 = 1.2$ which is closer to the exact solution for ∂D and $\lambda(\vartheta)$, respectively, than the initial guess $\boldsymbol{r}^0 = 0.6$ and $\boldsymbol{\lambda}^0 = 1$. Such a better initial guess could be inferred, prior to running the gradient-based routine `lsqnonlin`, by first optimizing the problem using a heuristic method, say a genetic algorithm-like optimizer, but this has not been undertaken in the current study. In Figures 8 and 9 we present the reconstructed boundary ∂D and impedance $\lambda(\vartheta)$, respectively, with no noise and no regularization after $1, 5, 100$ and 500 iterations. From these figures it can be seen that accurate reconstructions of both the scatterer and the impedance are obtained. Moreover, on comparing Figures 1 and 8, and Figures 5 and 9, we observe that the numerical reconstructions are very similar with only a slight decrease in accuracy when two instead of one unknown quantities are encountered. The corresponding results with `niter`=500, noise $p = 5\%$, $\mu_2 = \mu_3 = 0$ and regularization with μ_1, $\mu_1 = \mu_3 = 0$ and regularization with μ_2, and $\mu_1 = \mu_2 = 0$ and regularization with μ_3, for the scatterer and impedance are presented in Figures 10–15. From Figures 10, 12 and 14 it may be observed that regularization with either μ_1, μ_2 or μ_3 yields stable and accurate reconstructions of the unit disk, but the numerical results for the impedance function are more sensitive to the choice of the appropriate regularization parameter. In fact, Figure 15 shows that regularization with μ_3 fails to produce a reliable reconstruction of λ.

4.2. **Example 2.** We next consider the case of a peanut shape scatterer given by the radial parametrisation,

$$r(\vartheta) = \frac{1}{2}\sqrt{1 + 3\cos^2\vartheta}, \quad \vartheta \in [0, 2\pi). \tag{4.2}$$

We take $\boldsymbol{z}_0 = (0.25, 0)$ and λ given by (4.1).

4.2.1. *Inverse problem* A. All the discretization details are the same as in Example 1 except the initial guess $(\boldsymbol{c}^0, \boldsymbol{r}^0, \eta^0) = (\mathbf{0}, \mathbf{0.8}, 1.5)$. In Figure 16 we present the reconstructed boundary with no noise and no regularization after $1, 5, 100$ and 500 iterations. The corresponding results with `niter`=500, noise $p = 5\%$, $\mu_2 = 0$ and regularization with μ_1, and $\mu_1 = 0$ and regularization with μ_2, are presented in Figures 17 and 18, respectively. From these, conclusions similar to those obtained for Example 1 can be drawn.

4.2.2. *Inverse problem* B. In the implementation of this inverse problem we took the initial guess $(\boldsymbol{c}^0, \boldsymbol{\lambda}^0, \eta^0) = (\mathbf{0}, \mathbf{1.5}, 1.2)$ and $M = 50$. In Figure 19 we present the reconstructed impedance $\lambda(\vartheta)$ with no noise and no regularization after various numbers of iterations. The corresponding results with `niter`=500, noise $p = 5\%$, $\mu_3 = 0$ and regularization with μ_1, and $\mu_1 = 0$ and regularization with μ_3, are presented in Figures 20 and 21, respectively. When comparing Figures 5–7 with Figures 19–21 we observe that the numerical results for the impedance for Example 2 are less stable than those for Example 1.
The numerical results for inverse problem C for Example 2 were found to be inaccurate and are therefore not presented.

5. Conclusions

In this paper the MFS was used for the numerical solution of three inverse interior acoustic scattering problems. Since these are ill-posed problems, their discretized versions were regularized with respect to not only the magnitude of the MFS coefficients, but also the smoothness of the scatterer and the impedance function. The numerical results retrieved for two examples revealed that the method is well suited for the reconstruction of the unknown scatterer and impedance function even when the measured data was contaminated with noise. The three-dimensional case is straightforward after the corresponding modification of the fundamental solution in (2.1) and (3.2). Future work will concern the application of the MFS for the identification of an interior electromagnetic scatterer, [20]. The current state-of-the-art for inverse interior acoustic scattering is only for homogeneous media and an obvious

challenging and practical extension would be to, in the near future, analyse the detection of cavities in highly heterogeneous media.

References

[1] M. Belge, M. E. Kilmer, and E. L. Miller, *Efficient determination of multiple regularization parameters in a generalized L-curve framework*, Inverse Problems **18** (2002), 1161–1183.

[2] F. Cakoni and D. Colton, *Qualitative Methods in Inverse Scattering Theory*, Springer-Verlag, Berlin, 2006.

[3] D. Colton and R. Kress, *Inverse Acoustic and Electromagnetic Scattering Theory*, second ed., Applied Mathematical Sciences, vol. 93, Springer-Verlag, Berlin, 1998.

[4] D. Colton and R. Kress, *Using fundamental solutions in inverse scattering*, Inverse Problems **22** (2006), R49–R66.

[5] G. Fairweather, A. Karageorghis, and P. A. Martin, *The method of fundamental solutions for scattering and radiation problems*, Eng. Anal. Bound. Elem. **27** (2003), 759–769.

[6] P. Jakubik and R. Potthast, *Testing the integrity of some cavity - the Cauchy problem and the range test*, Appl. Numer. Math. **58** (2008), 899–914.

[7] A. Karageorghis, D. Lesnic, and L. Marin, *A moving pseudo-boundary MFS for void detection*, Numer. Methods Partial Differential Equations **29** (2013), 935–960.

[8] A. Karageorghis, B. Bin-Mohsin, D. Lesnic and L. Marin, *Simultaneous numerical determination of a corroded boundary and its admittance*, Inverse Problems Sci. Eng. **23** (2015), 1120–1137.

[9] A. Karageorghis, D. Lesnic and L. Marin, *The MFS for the identification of a sound-soft interior acoustic scatterer*, (2017) submitted.

[10] A. Karageorghis, D. Lesnic and L. Marin, *The PWM for the identification of a sound-soft interior acoustic scatterer*, in L. Marin and M. H. Aliabadi, Editors, *Advances in Boundary Element and Meshless Techniques XVIII*, EC Ltd, UK, 2017, pp 19-26.

[11] R. Kress, *Newton's method for inverse obstacle scattering meets the method of least squares*, Inverse Problems **19** (2003), S91–S104.

[12] P. Li and Y. Wang, *Near-field imaging of interior cavities*, Commun. Comput. Phys. **17** (2015), 542–563.

[13] P. Li and Y. Wang, *Near-field imaging of obstacles*, Inverse Problems and Imaging **9** (2015), 189–210.

[14] P. Li and Y. Wang, *Numerical solution of an inverse scattering problem with near-field data*, J. Comput. Phys. **290** (2015), 157–168.

[15] X. Liu, *The factorization method for cavities*, Inverse Problems **30** (2014), 015006 (18 pp).

[16] The MathWorks, Inc., 3 Apple Hill Dr., Natick, MA, *Matlab*.

[17] H.-H. Qin and F. Cakoni, *Nonlinear integral equations for shape reconstruction in the inverse interior scattering problem*, Inverse Problems **27** (2011), 035005 (17 pp).

[18] H.-H. Qin and D. Colton, *The inverse scattering problem for cavities*, Appl. Numer. Math. **62** (2012), 699–708.

[19] H.-H. Qin and D. Colton, *The inverse scattering problem for cavities with impedance boundary condition*, Adv. Comput. Math. **36** (2012), 157–174.

[20] F. Zeng, F. Cakoni and J. Sun, *An inverse electromagnetic scattering problem for a cavity*, Inverse Problems **27** (2011), 125002 (17 pp).

[21] F. Zeng, P. Suarez and J. Sun, *A decomposition method for an interior scattering problem*, Inverse Problems and Imaging **7** (2013), 291–303.

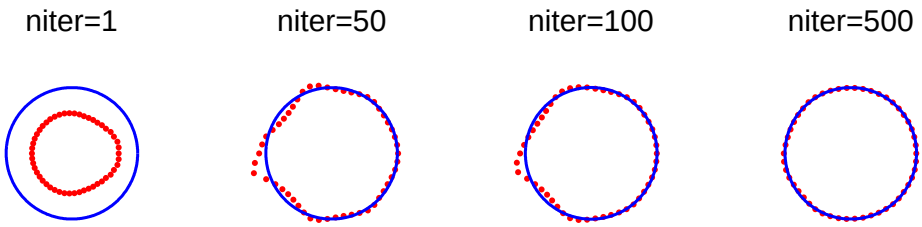

FIGURE 1. Example 1, Problem A: Results for scatterer for $M = 50, L = 32$, no noise and no regularization for various numbers of iterations.

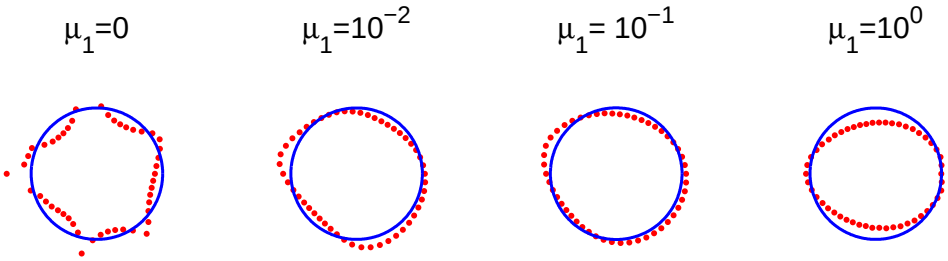

FIGURE 2. Example 1, Problem A: Results for scatterer for $M = 50, L = 32$, noise $p = 5\%$, $\mu_2 = 0$ and regularization with μ_1.

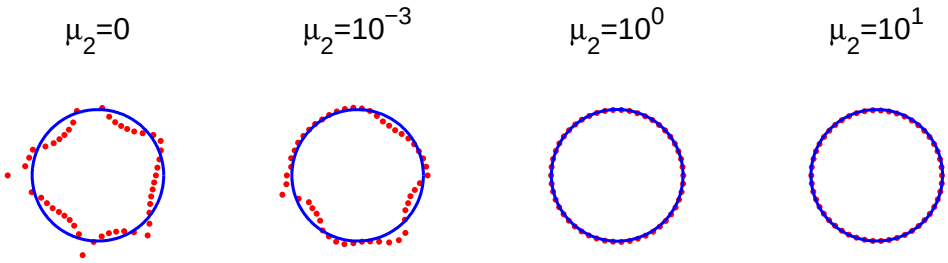

FIGURE 3. Example 1, Problem A: Results for scatterer for $M = 50, L = 32$, noise $p = 5\%$, $\mu_1 = 0$ and regularization with μ_2.

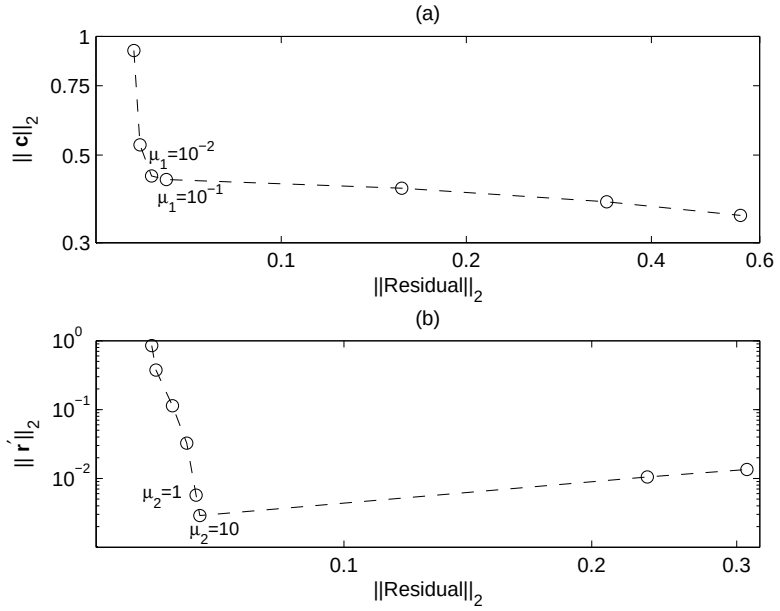

FIGURE 4. Example 1, Problem A: L-curves for $p = 5\%$. (a) Varying μ_1 with $\mu_2 = 0$; (a) Varying μ_2 with $\mu_1 = 0$.

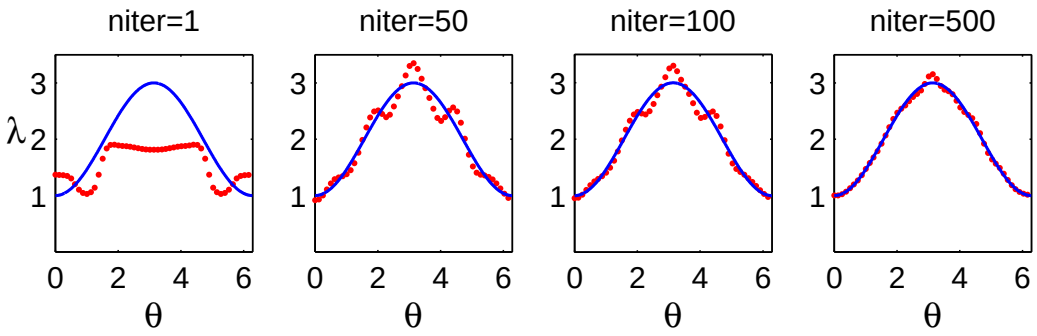

FIGURE 5. Example 1, Problem B: Results for impedance for $M = 50, L = 32$, no noise and no regularization for various numbers of iterations.

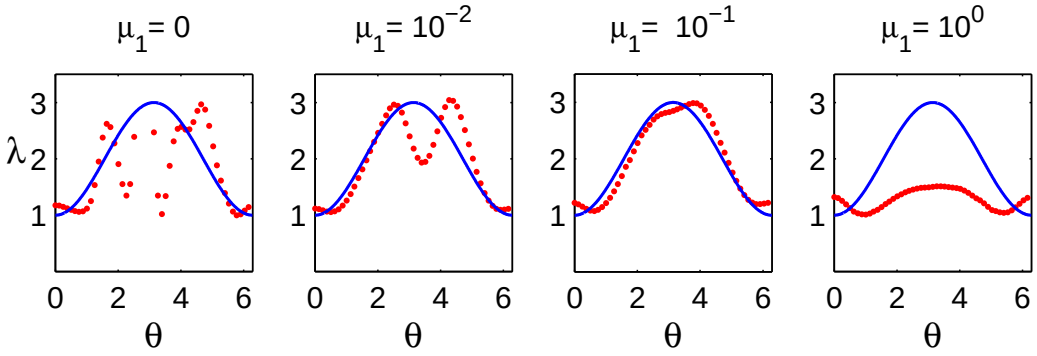

FIGURE 6. Example 1, Problem B: Results for impedance for $M = 50, L = 32$, noise $p = 5\%$, $\mu_3 = 0$ and regularization with μ_1.

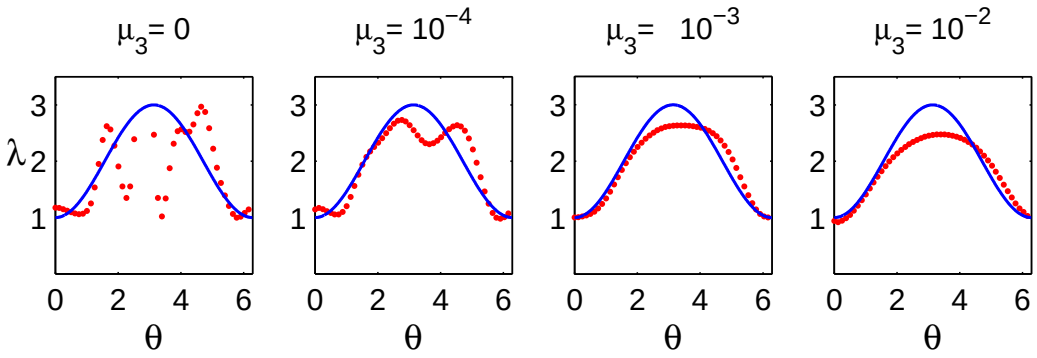

FIGURE 7. Example 1, Problem B: Results for impedance for $M = 50, L = 32$, noise $p = 5\%$, $\mu_1 = 0$ and regularization with μ_3.

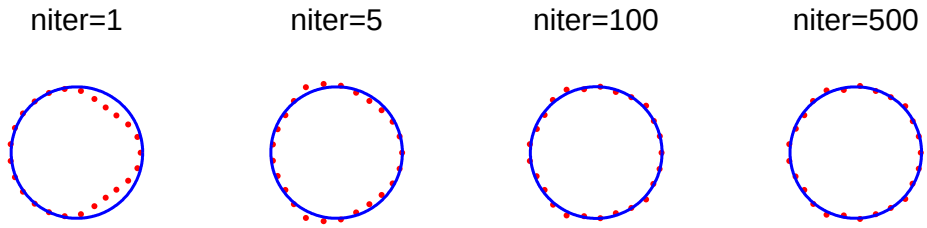

FIGURE 8. Example 1, Problem C: Results for scatterer for $M = 25, L = 32$, no noise and no regularization for various numbers of iterations.

DEPARTMENT OF MATHEMATICS AND STATISTICS, UNIVERSITY OF CYPRUS/ ΠΑΝΕΠΙΣΤΗΜΙΟ ΚΥΠΡΟΥ, P.O.BOX 20537, 1678 NICOSIA/ΛΕΥΚΩΣΙΑ, CYPRUS/ΚΥΠΡΟΣ
E-mail address: andreask@ucy.ac.cy

DEPARTMENT OF APPLIED MATHEMATICS, UNIVERSITY OF LEEDS, LEEDS LS2 9JT, UK
E-mail address: amt5ld@maths.leeds.ac.uk

DEPARTMENT OF MATHEMATICS, FACULTY OF MATHEMATICS AND COMPUTER SCIENCE, UNIVERSITY OF BUCHAREST, 14 ACADEMIEI, 010014 BUCHAREST, AND INSTITUTE OF MATHEMATICAL STATISTICS AND APPLIED MATHEMATICS, ROMANIAN ACADEMY, 13 CALEA 13 SEPTEMBRIE, 050711 BUCHAREST, ROMANIA
E-mail address: marin.liviu@gmail.com; liviu.marin@fmi.unibuc.ro

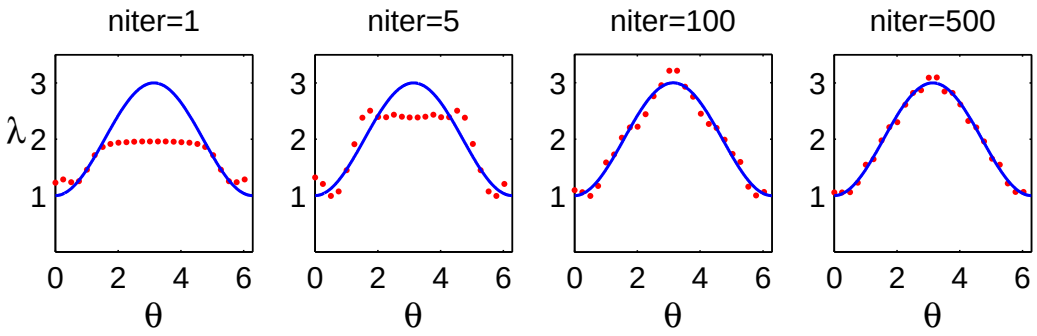

FIGURE 9. Example 1, Problem C: Results for impedance for $M = 25, L = 32$, no noise and no regularization for various numbers of iterations.

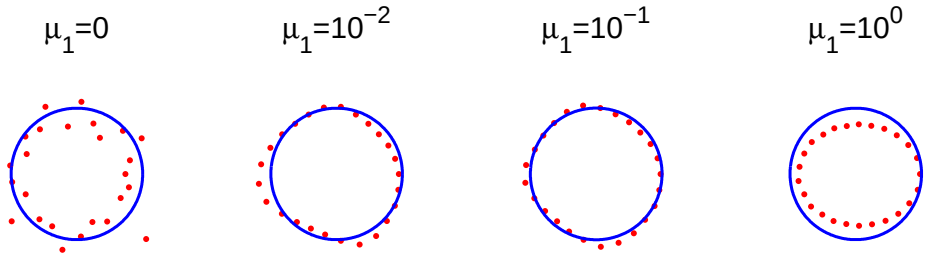

FIGURE 10. Example 1, Problem C: Results for scatterer for $M = 25, L = 32$, noise $p = 5\%$, $\mu_2 = \mu_3 = 0$ and regularization with μ_1.

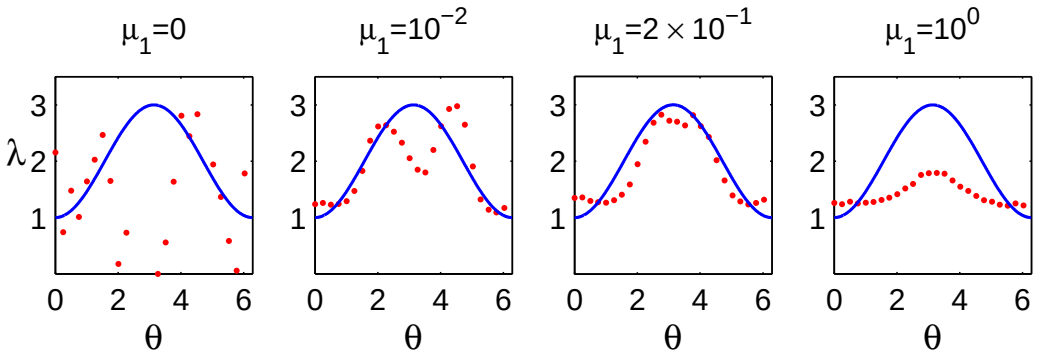

FIGURE 11. Example 1, Problem C: Results for impedance for $M = 25, L = 32$, noise $p = 5\%$, $\mu_2 = \mu_3 = 0$ and regularization with μ_1.

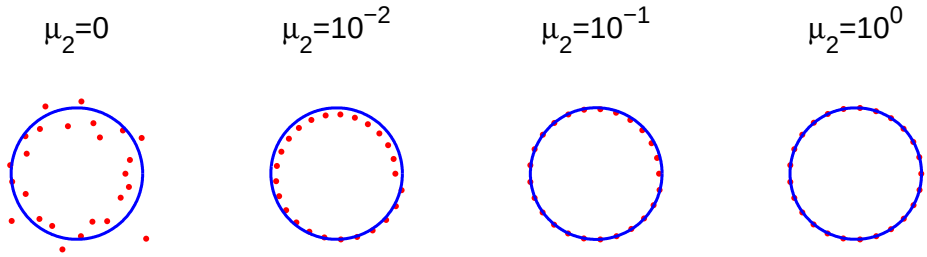

FIGURE 12. Example 1, Problem C: Results for scatterer for $M = 25, L = 32$, noise $p = 5\%$, $\mu_1 = \mu_3 = 0$ and regularization with μ_2.

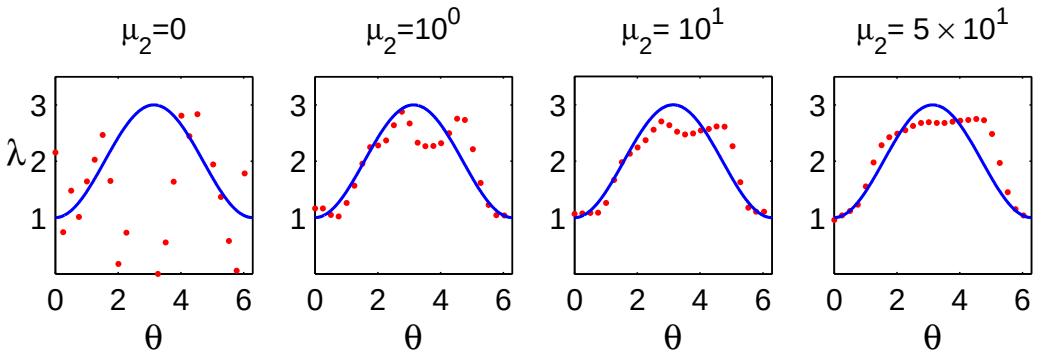

FIGURE 13. Example 1, Problem C: Results for impedance for $M = 25, L = 32$, noise $p = 5\%$, $\mu_1 = \mu_3 = 0$ and regularization with μ_2.

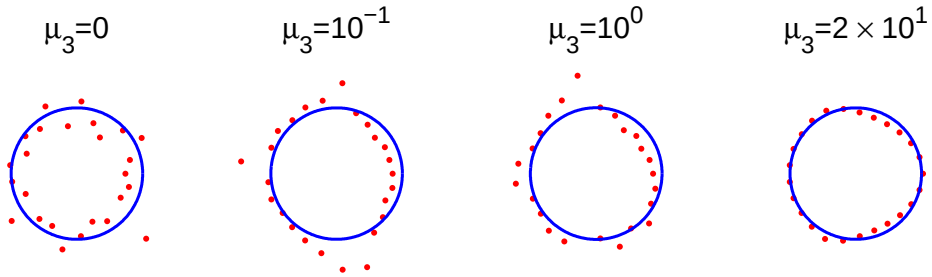

FIGURE 14. Example 1, Problem C: Results for scatterer for $M = 25, L = 32$, noise $p = 5\%$, $\mu_1 = \mu_2 = 0$ and regularization with μ_3.

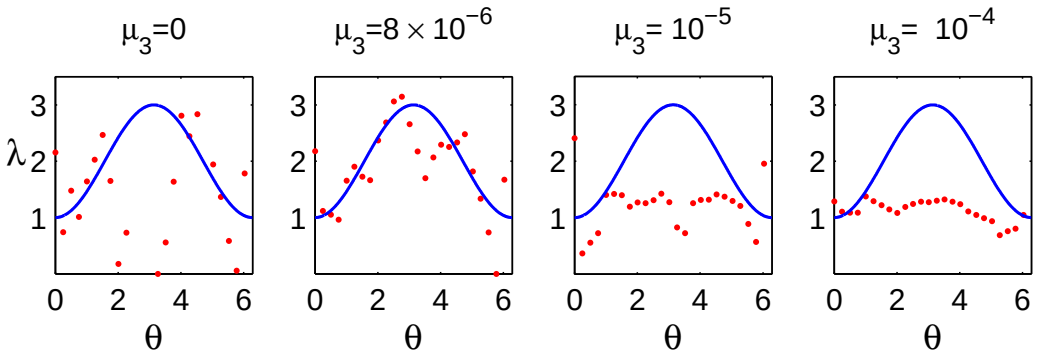

FIGURE 15. Example 1, Problem C: Results for impedance for $M = 25, L = 32$, noise $p = 5\%$, $\mu_1 = \mu_2 = 0$ and regularization with μ_3.

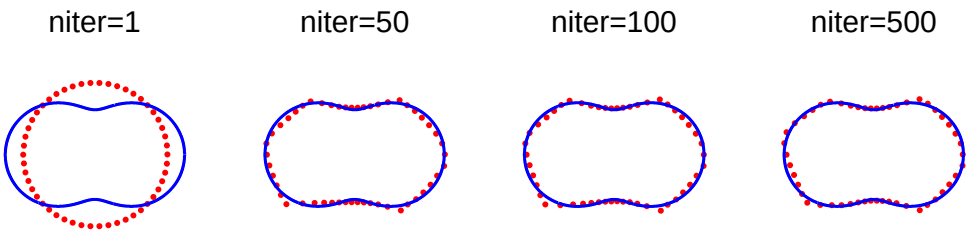

FIGURE 16. Example 2, Problem A: Results for scatterer for $M = 50, L = 32$, no noise and no regularization for various numbers of iterations.

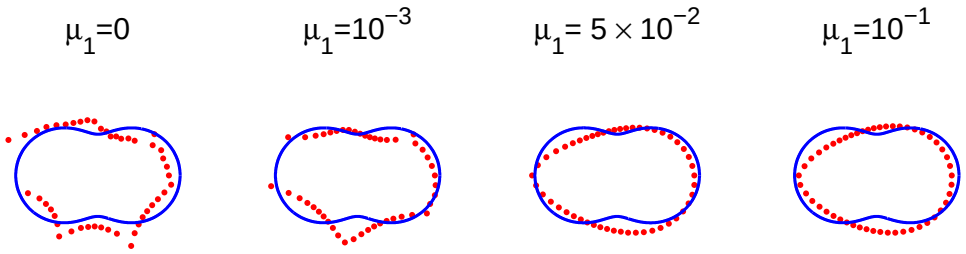

FIGURE 17. Example 2, Problem A: Results for scatterer for $M = 50, L = 32$, noise $p = 5\%$, $\mu_2 = 0$ and regularization with μ_1.

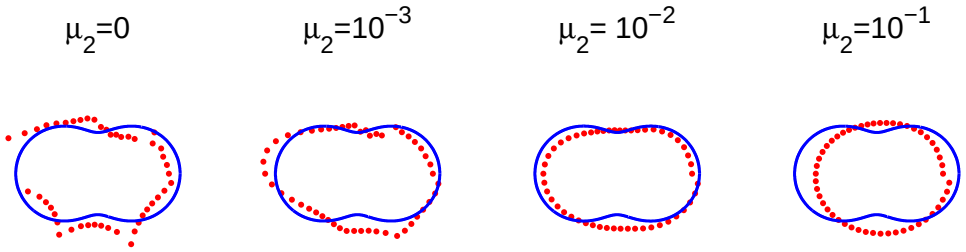

FIGURE 18. Example 2, Problem A: Results for scatterer for $M = 50, L = 32$, noise $p = 5\%$, $\mu_1 = 0$ and regularization with μ_2.

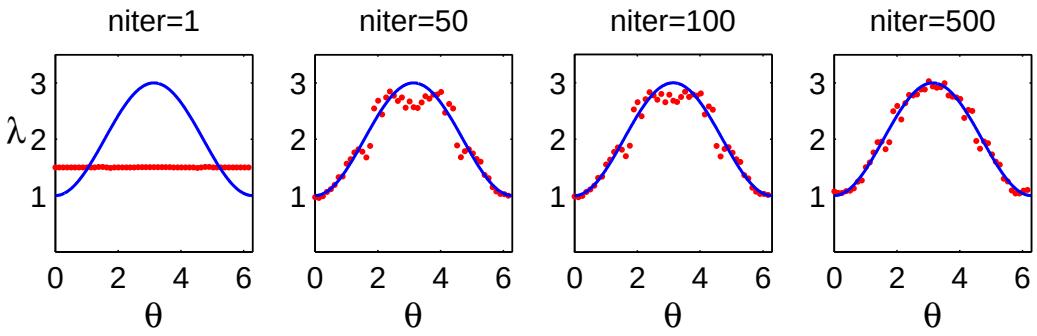

FIGURE 19. Example 2, Problem B: Results for impedance for $M = 50, L = 32$, no noise and no regularization for various numbers of iterations.

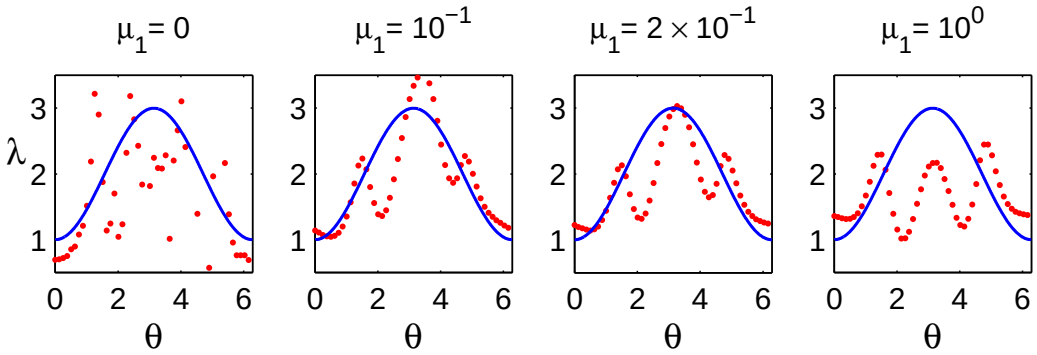

FIGURE 20. Example 2, Problem B: Results for impedance for $M = 50, L = 32$, noise $p = 5\%$, $\mu_3 = 0$ and regularization with μ_1.

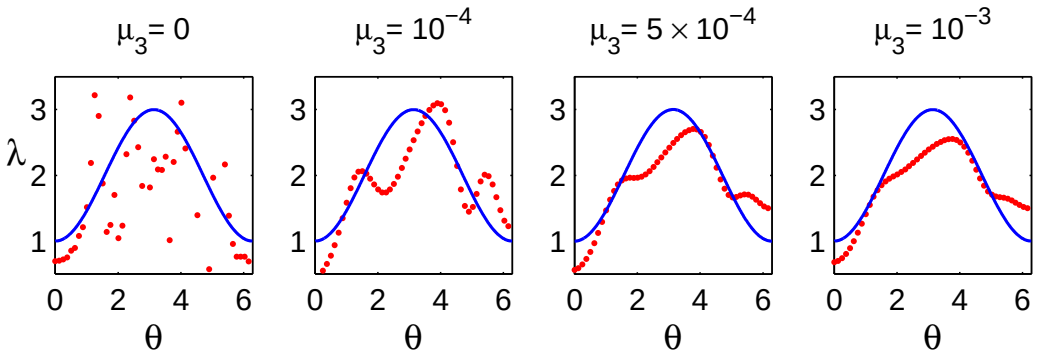

FIGURE 21. Example 2, Problem B: Results for impedance for $M = 50, L = 32$, noise $p = 5\%$, $\mu_1 = 0$ and regularization with μ_3.